

Evidence for Core-Core Collision in Barnard 68

DALEI LI,^{1,2,3} CHRISTIAN HENKEL,^{4,1} ALEXANDER KRAUS,⁴ XINDI TANG,^{1,2,3,5} WILLEM BAAN,¹ JARKEN ESIMBEK,^{1,2,3,5}
KE WANG,⁶ GANG WU,^{1,3} TIE LIU,⁷ ANDREJ M. SOBOLEV,^{8,1} JIANJUN ZHOU,^{1,3,5} YUXIN HE,^{1,2,3} AND
TOKTARKHAN KOMESH^{9,10}

¹*Xinjiang Astronomical Observatory, Chinese Academy of Sciences, Urumqi 830011, People's Republic of China*

²*University of Chinese Academy of Sciences, Beijing 100049, People's Republic of China*

³*Xinjiang Key Laboratory of Radio Astrophysics, Urumqi 830011, People's Republic of China*

⁴*Max-Planck-Institut für Radioastronomie, Auf dem Hügel 69, D-53121 Bonn, Germany*

⁵*Key Laboratory of Radio Astronomy and Technology, Chinese Academy of Sciences, A20 Datun Road, Chaoyang District, Beijing, 100101, P. R. China*

⁶*Kavli Institute for Astronomy and Astrophysics, Peking University, Beijing 100871, People's Republic of China*

⁷*Shanghai Astronomical Observatory, Chinese Academy of Sciences, 80 Nandan Road, Shanghai 200030, People's Republic of China*

⁸*Ural Federal University, 19 Mira Street, 620002 Ekaterinburg, Russia*

⁹*Energetic Cosmos Laboratory, Nazarbayev University, Astana 010000, Kazakhstan*

¹⁰*Institute of Experimental and Theoretical Physics, Al-Farabi Kazakh National University, Almaty 050040, Kazakhstan*

Submitted to ApJ

ABSTRACT

The prestellar core Barnard 68 (B68) is a prototypical source to study the initial conditions and chemical processes of star formation. A previous numerical simulation suggested the southeastern bullet is impacting on the main body of B68. In order to obtain more observational evidence, mapping observations of the ground state SO ($1_0 - 0_1$) emission line at 30 GHz were made with the Effelsberg 100m telescope. Based on the velocity field and channel maps derived from SO, three velocity components were clearly detected. The velocity field of the main body indicates rotation and is well fitted by a solid-body rotation model. The measured radial velocity difference between the bullet and the main core is about 0.4 km s^{-1} , which is almost equal to the velocity obtained by the previous numerical simulation. Therefore, the bullet is most likely impacting onto the rotating main body of B68. A 1D spherical non-LTE Monte-Carlo radiation transfer RATRAN code is performed to derive the radial abundance profile of SO by analyzing the observed velocity-integrated intensity. SO is depleted inside a $60''$ (0.02 pc) radius from the core. The abundance stays constant at 2.0×10^{-9} for radii larger than $60''$ from the center of the main core. The abundance is enhanced at the interface of the bullet and the main core indicating that shock waves were produced by the collision between the bullet and the main core. In conclusion, based on the kinematical and chemical analysis, our observational results support the previously proposed core-core collision scenario in B68.

Keywords: ISM: abundances – ISM: clouds – ISM: kinematics and dynamics – ISM: molecules – ISM: individual objects: B68 – radio Lines: ISM

1. INTRODUCTION

Stars are generally believed to be formed from dense collapsing molecular cores. Observations towards dense molecular cores can help us to understand the initial

conditions and early stages of star formation (Bergin & Tafalla 2007; McKee & Ostriker 2007). Especially, isolated dense molecular cores are ideal targets for testing star-forming theories, such as Barnard 68 (B68; Barnard 1919), which is a small and isolated Bok globule (Bok & Reilly 1947). Because of its simple and at first sight almost spherical structure, B68 is a perfect source to study the initial conditions of star formation.

Based on near-infrared observations and dust extinction studies (Lada et al. 1994), Alves et al. (2001b) derived the column density structure of B68 with high sensitivity and spatial resolution. They then found that the column density structure is well fitted by a Bonnor-Ebert sphere (Bonnor 1956; Ebert 1955) with a fitted parameter $\xi_{\max} = 6.9 \pm 0.2$ (Alves et al. 2001b, see Appendix A). This model involving thermal pressure dominating against gravity was supported by follow-up molecular line observations. For example, NH_3 data observed with the Effelsberg 100 m telescope (Hotzel et al. 2002) show extremely narrow full width to half maximum (FWHM) line widths of $0.181 \pm 0.003 \text{ km s}^{-1}$. Such narrow line widths were also detected by follow-up observations of other molecules in B68, for C^{18}O , about $0.18 \pm 0.01 \text{ km s}^{-1}$, and for C^{34}S , about $0.15 \pm 0.01 \text{ km s}^{-1}$ (Lada et al. 2003). The estimated sonic Mach numbers (ratios of the nonthermal velocity dispersion with respect to sound speed), are 0.17 for NH_3 , 0.30 for C^{18}O and 0.25 for C^{34}S assuming the gas kinetic temperature of 10 K. Distance estimates for B68 range from 60 to 205 pc (de Geus et al. 1989; Hotzel et al. 2002; Lai et al. 2003; Lombardi et al. 2006; Alves & Franco 2007). In order to fit the B68 density structure with a Bonnor-Ebert sphere at 10 K, a distance of 78 pc is adopted in the following (Hotzel et al. 2002; Lai et al. 2003; Li et al. 2018).

The internal motions and dynamical state of B68 can be deduced from molecular line observations. Lada et al. (2003) performed high spatial resolution C^{18}O (1-0), N_2H^+ (1-0), C^{32}S (2-1) and C^{34}S (2-1) molecular emission line mapping observations using the IRAM (Institut de Radioastronomie Millimétrique) 30 m telescope. In contrast to the C^{34}S single peak line profiles, C^{32}S (2-1) shows complex blueshifted and red-shifted profiles so-called 'self-reversed' line structure revealing that B68 contains very complex motions indicating non-radial oscillations (Lada et al. 2003). Soon after, the non-radial oscillations were also detected by follow-up JCMT (James Clerk Maxwell Telescope) HCO^+ (3-2) mapping observations (Redman et al. 2006). In additional studies, many molecular lines were detected including ^{13}CO , C^{18}O , HCO^+ , H^{13}CO^+ , DCO^+ , N_2H^+ and more complex motions inside the core were revealed (Maret et al. 2007). For example, at the core center, they found that molecular transitions tracing particularly dense gas, HCO^+ (4-3), DCO^+ (3-2) and N_2H^+ (1-0), show a red asymmetry indicating expansion while HCO^+ (1-0) and (3-2) show a blue asymmetry, revealing radial oscillations at the core center of B68 (Maret et al. 2007). Because B68 is experiencing non-radial and radial oscillations (Keto et al. 2006; Redman et al.

2006; Maret et al. 2007), its core could be more stable and much more long-lived, about 3×10^6 years, than suggested by the free-fall timescale of 1.7×10^5 years (Burkert & Alves 2009).

However, as mentioned above, the fitted parameter $\xi_{\max} = 6.9 \pm 0.2$ (Alves et al. 2001b) is slightly larger than the critical value of $\xi_{\max} = 6.5$ for a Bonnor-Ebert sphere model indicating that B68 may be unstable and collapse with a freefall timescale (Burkert & Alves 2009; Li et al. 2018). In order to resolve this contradiction, Burkert & Alves (2009) proposed a core-core collision scenario and did a simulation that the smaller core at the southeastern corner of B68 is impacting on the main body, initiating and accelerating gravitational collapse. In the numerical simulation, the impact velocity is with 0.37 km s^{-1} supersonic and the supersonic fluid may produce shock waves.

SO is an excellent tracer to study a cold dark cloud and to trace shock waves. There are many cold dark clouds already mapped by the ground transition $\text{SO}(1_0 - 0_1)$. For example, Rydbeck et al. (1980) performed SO observations toward many dark molecular clouds with a $2'$ resolution, Heithausen et al. (1995) inspected galactic cirrus, Codella & Muders (1997) studied Bok globules and Lique et al. (2006) observed TMC-1. Besides, SO is also a good species to trace shock waves which can significantly enhance the SO abundance. By performing SO observations, Martin-Pintado et al. (1992) already mapped L1448 and Cep A in both ambient quiescent and shocked outflow regions and found $[\text{SO}/\text{H}_2]$ ratios being enhanced, with fractional abundances of quiescent gas, 0.9×10^{-9} , to that of shocked regions, $> 15 \times 10^{-9}$ for L1448 and 1.8×10^{-9} to $> 13 \times 10^{-9}$ for Cep A (Blake et al. 1987; Schilke et al. 1997; Comito et al. 2005). Friberg (1984) mapped the Orion KL region using the SO emission and found that the SO abundance is enhanced to 2×10^{-6} in the active regions of Orion KL, while the ambient abundance of SO is only 0.3% that of the active regions. Schmid-Burgk et al. (1992) even found strong SO emission where CO is absent, located in some regions of the blue lobe of the L1221 outflow. There exists a strong correlation between SO spots and the endpoints of molecular outflows (Schmid-Burgk & Muders 1994; Chuang et al. 2021). Therefore, SO is likely a potential ideal tracer to test the core-core collision scenario towards the prototypical Bok globule B68.

2. OBSERVATIONS AND DATA ARCHIVE

Mapping observations of the SO(1_0-0_1) molecular emission line at 30.00154 GHz¹ (F.J.Lovas, private communication, Remijan et al. 2007) were made with the Effelsberg 100 m telescope² by adopting the On-The-Fly (OTF) in position switching mode in March, 2017. The spatial angular resolution is 30". In order to increase the signal-to-noise ratios in individual channels, the data were smoothed to 40" (~ 0.015 pc). The prime focus receiver P10mm (4-Box) with a frequency coverage of 27.0 – 38.5 GHz was selected. An XFFT (FFT: Fast Fourier Transform) spectrometer with 32768 spectral channels and a bandwidth of 400 MHz, corresponding to a channel width of 0.036 km s^{-1} , has been employed. The data were reduced by the CLASS package of GILDAS³. All spectra were individually corrected for the atmospheric attenuation and the gain-elevation effect of the antenna (loss of sensitivity due to gravitational deformation during tilt). For the final calibration into K, T_{MB} conversion factors were derived by observing suitable calibrators (NGC 7027) in continuum (Winkel et al. 2012). The uncertainties are of the order of 10%.

In addition to the molecular SO line data, a DSS (Digitized Sky Surveys) image was retrieved from the ESO data archive⁴.

3. RESULTS

3.1. The spectral SO lines

The upper panel in Fig. 1 presents the observed spectral line of SO towards the dust extinction peak of B68 (Bergin et al. 2002). Contrary to the complex line profiles detected in HCO^+ (1-0), (3-2), (4-3), DCO^+ (2-1) and (3-2) (see Fig. 1 of Maret et al. 2007), the SO shows a single profile.

The lower panel in Fig. 1 shows the observed SO line profiles. Both the main body and the southeastern bullet are clearly detected. Not only the spectrum towards the column density peak, but all spectra show single Gaussian profiles, which are quite different from the previous mapping results of asymmetric, self-reversed line profiles as seen in the CS (2-1) and HCO^+ (3-2) lines obtained by the IRAM 30 m and JCMT 15 m, respectively (Lada et al. 2003; Redman et al. 2006).

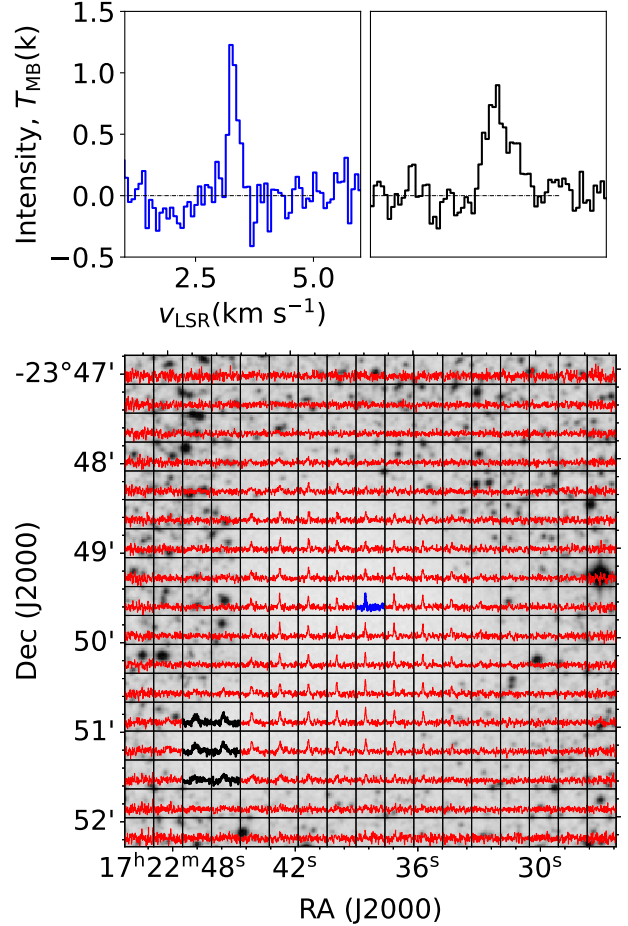


Figure 1. Observed SO spectra. Upper panel (left): The SO spectrum towards the column density peak ($\alpha_{\text{J2000}} = 17:22:38.60$, $\delta_{\text{J2000}} = -23:49:46.0$) presented with a Local Standard of Rest velocity scale. Upper panel (right): The averaged spectra derived from six spectral lines (black) in the tail region of the core. The x- and y-axis scales are identical to those of the spectra on the left. Bottom panel: The spectral line map overlaid on a negative Digital Sky Survey (DSS) image, with white indicating the morphology of the globule and black representing stellar objects in the outskirts of the image. The profiles of the upper panel are emphasized in the middle and at the bottom left of the lower panel, respectively.

3.2. The spatial distribution of SO

To investigate the spatial distribution and kinematics of SO, the commonly used moment method was performed to derive the velocity-integrated intensity distribution (moment-0), the intensity-weighted velocity field (moment-1) and the intensity-weighted velocity dispersion field (moment-2). The integrated LSR velocities range from 3.0 to 3.8 km s^{-1} . The velocity-integrated

¹ This value was taken from the Spectral Line Atlas of Interstellar Molecules (SLAIM) (Available at <https://splatalogue.online/#/basic>).

² This work is based on observations with the 100-m telescope of the MPIfR (Max-Planck-Institut für Radioastronomie) at Effelsberg.

³ <http://www.iram.fr/IRAMFR/GILDAS>

⁴ <https://archive.eso.org/dss/dss>

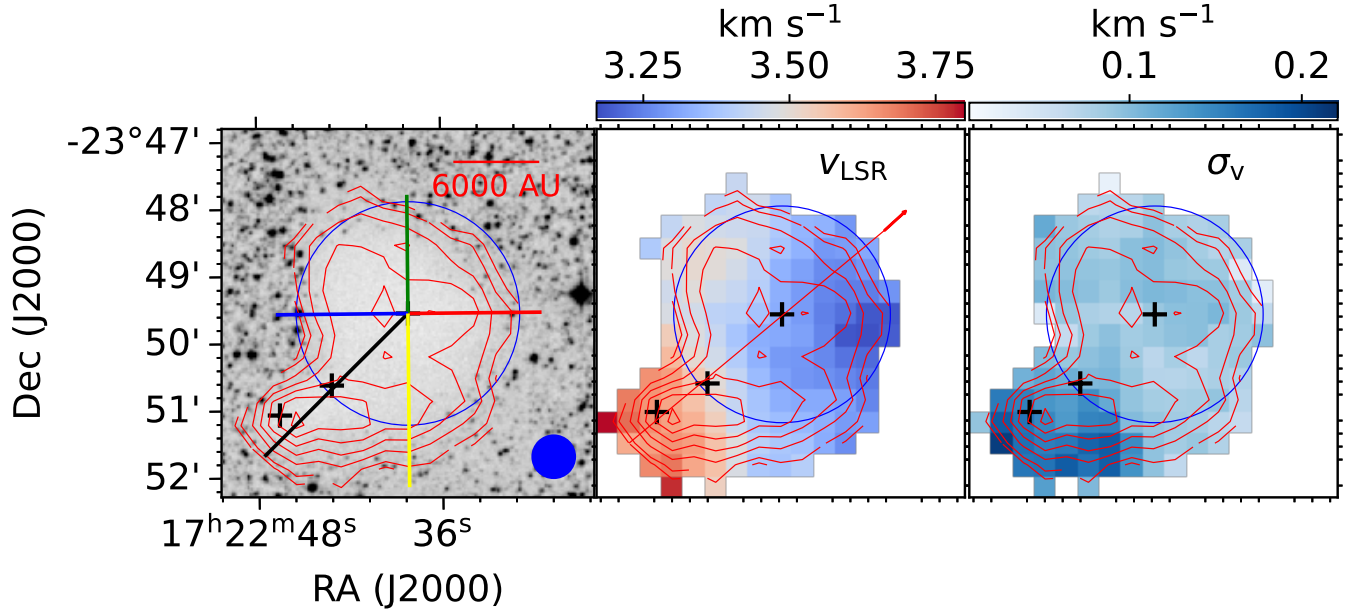


Figure 2. The spatial distribution of SO. Velocity-integrated intensity contour map of B68 overlaid on the Digitized Sky Survey (DSS) image. The blue circle with a radius of $100''$ marks the main body of B68 (Alves et al. 2001b). The plus symbols show the peaks of the three dust cores detected by the dust extinction measurements with an angular resolution of $10''$ (see Fig. 7 dust extinction map of Alves et al. 2001a). Left: The red contours show the $\text{SO}(1_0 - 0_1)$ molecular line emission. The contour levels start from 2σ ($\sigma = 0.036 \text{ K km s}^{-1}$) with an interval 2σ . The beam size (blue filled circle) is shown in the lower right corner of the left panel. The various straight lines show the paths to extract the velocity-integrated intensity distribution presented in Fig. 4. The middle panel marks the velocity field distribution. The red line is the path for the position-velocity diagram in Fig. 5. The right panel presents the velocity dispersion σ_v .

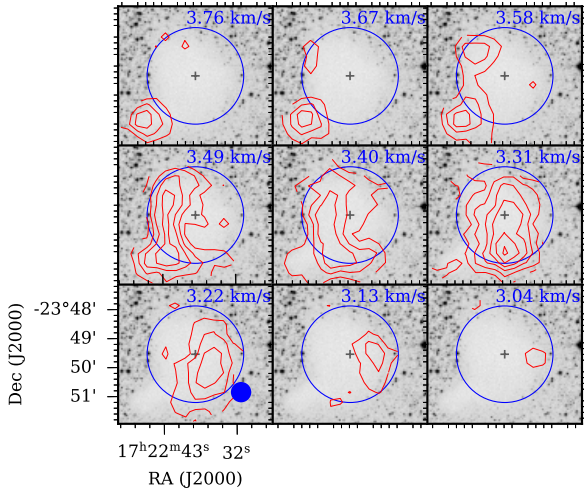


Figure 3. kinematic component decomposition. Channel maps of SO (red contours) overlaid on the DSS image (see Fig. 1). Levels start from 3σ ($\sigma = 0.012 \text{ K km s}^{-1}$) with an interval of 3σ . The blue circles mark the main body of B68. The beam size is shown in the bottom right corner of the bottom left panel.

panel of Fig. 2. The strongest emission of SO is located at the southeastern part instead of the centrally located column density peak detected by the dust extinction measurements with an angular resolution of $10''$ (Alves et al. 2001a,b). The central region near the core shows lower velocity integrated intensities. A similar morphology is detected by CS emission line observations (Lada et al. 2003).

The middle panel in Fig. 2 shows the velocity field (moment-1) of SO. Three velocity components are clearly detected. The western part shows the lowest velocity component, and the southeastern part shows the highest velocity component, while the eastern part provides intermediate velocities. The three parts including the bullet and the red- and blueshifted parts of the main body are clearly arising from different regions as can be inferred from the channel maps in Fig. 3.

The right panel in Fig. 2 shows the velocity dispersion (moment-2) of SO. The main core of B68 shows a quite constant velocity dispersion, around 0.09 km s^{-1} . The southeastern core shows a larger velocity dispersion, at the order of 0.16 km s^{-1} .

intensity (moment-0) maps of B68 are shown in the left

4. DISCUSSION

4.1. Solid-body rotation of B68

The velocity gradients detected by molecular lines of C^{18}O and N_2H^+ in B68 have been explained with the solid-body rotation model (Lada et al. 2003). The middle panel in Fig. 2 shows a similar velocity gradient as those seen in C^{18}O and N_2H^+ (Lada et al. 2003). Therefore, the solid-body rotation is well traced by the SO.

The parameters to describe the solid-body rotation can be fitted towards the velocity field measured with SO using the following equation (Goodman et al. 1993; Lada et al. 2003)

$$v_{\text{lsr}} = v_{\text{sys}} + \frac{dv}{ds} \Delta \text{RA} \cos(\theta) + \frac{dv}{ds} \Delta \text{DEC} \sin(\theta), \quad (1)$$

where v_{lsr} is the observed line of sight velocity in units of km s^{-1} , v_{sys} is the systemic velocity of the core in units of km s^{-1} , dv/ds is the velocity gradient in units of $\text{km s}^{-1} \text{ arcsec}^{-1}$, θ is its direction in units of degrees (e.g., $\theta=0$ degrees: velocities rise towards the east; $\theta=90$ degrees: velocities increase towards the north). ΔRA and ΔDEC are the offsets in right ascension and declination in units of arcsec. In summary, v_{sys} , dv/ds and θ are the three free parameters and can be determined by fitting the observed velocity field presented in the middle panel of Fig. 2.

In order to obtain the best-fitting parameters, the MCMC (Markov chain Monte Carlo) procedure is used with the python-based code emcee⁵ (Goodman & Weare 2010). The implementation details for the emcee code are provided in Appendix B. The posterior distributions of the three free parameters are shown in Fig. 6. The best-fitting parameters are $v_{\text{sys}} = 3.362 \pm 0.001 \text{ km s}^{-1}$, $dv/ds = 1.79 \pm 0.02 \text{ m s}^{-1} \text{ arcsec}^{-1}$ and $\theta = 1^\circ 68 \pm 0^\circ 72$. Compared to the previous results obtained with C^{18}O and N_2H^+ (Lada et al. 2003), the velocity gradient dv/ds and the direction θ are consistent with the values $1.72 \pm 0.09 \text{ m s}^{-1} \text{ arcsec}^{-1}$ for N_2H^+ and $5^\circ 5 \pm 1^\circ 2$ for C^{18}O , respectively, but there are different with the values $2.25 \pm 0.024 \text{ m s}^{-1} \text{ arcsec}^{-1}$ for C^{18}O and $23^\circ 5 \pm 1^\circ 2$ for N_2H^+ . The v_{sys} derived here is consistent with the values 3.3722 ± 0.0018 and $3.3614 \pm 0.0009 \text{ km s}^{-1}$ derived from N_2H^+ and C^{18}O , respectively (Lada et al. 2003).

4.2. Radial distribution of SO abundances

The abundance profile of SO is derived from the velocity-integrated intensity by performing a non-LTE (Local Thermodynamic Equilibrium) radiation transfer calculation. The non-LTE radiation transfer is done

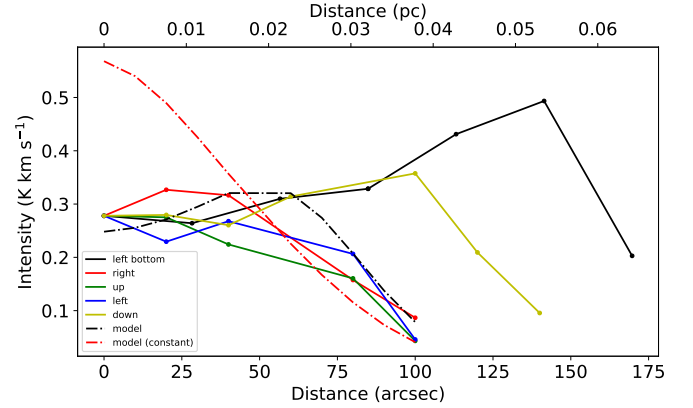


Figure 4. Comparison of observed and simulated intensity profiles. The radial profiles of velocity-integrated intensity from the column density peak (Fig. 1) along the five directions shown in the left panel in Fig. 2 and the simulated velocity-integrated intensity derived from the non-LTE radiation transfer code RATRAN (Hogerheijde & van der Tak 2000) with non-constant (black dash-dotted line) and constant (red dash-dotted line) SO abundance distributions.

with the Monte Carlo code RATRAN⁶ under 1D spherically symmetry (Hogerheijde & van der Tak 2000). The molecular data file of SO was taken from the Leiden Atomic and Molecular Database (LAMDA; Lique et al. 2006)

For the non-LTE radiation transfer calculation, the density structure is the Bonner-Ebert sphere with $\xi_{\text{max}} = 6.9$ well determined by the dust extinction data (Alves et al. 2001b). The gas kinetic temperature is about 10 K derived from NH_3 (J,K) = (1,1) and (2,2) data obtained with the Effelsberg 100 m telescope (Hotzel et al. 2002). Therefore, both the gas and dust temperatures are set to 10 K for the calculation. From the right panel in Fig. 2, the velocity dispersion for the main core of B68 is about 0.09 km s^{-1} .

In Fig. 4, the velocity-integrated intensity of SO firstly increases from the core center to then decline towards the boundary. This follows the trend of SO velocity-integrated intensity also seen in L1498 and L1517B (Tafalla et al. 2006). Therefore, a step function is adopted to describe the radial abundance profile of SO for B68. SO is depleted at the core center, while the abundance keeps constant for larger radii (Tafalla et al. 2006).

A synthetic SO spectral line cube is produced from the non-LTE radiation transfer. Then the cube is convolved with a $40''$ FWHM Gaussian. The convolved

⁵ <https://emcee.readthedocs.io/en/latest/>

⁶ <https://sronpersonalpages.nl/~vdtak/ratran/frames.html>

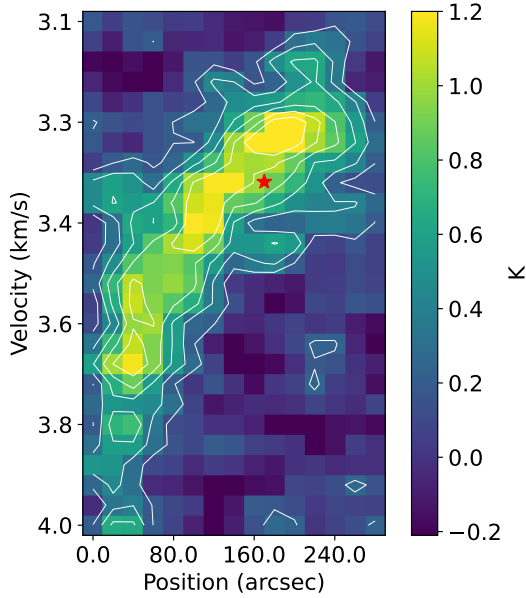


Figure 5. Impact velocity estimation between the bullet and the main core. Position-Velocity diagram along the red straight line from the bottom left to the upper right shown in the middle panel in Fig. 2. The white contours represent the intensity of SO and the contour levels start from 0.2 to 1.2 K with an interval of 0.2 K. The red star shows the location of the column density peak of the main core.

cube is used to produce velocity-integrated intensities and is then compared to the observational results. Fig. 4 compares the radial profiles of velocity-integrated intensity with the simulated intensity by RATRAN if the abundances are zero for radii less than $60''$ (0.02 pc) and 2.0×10^{-9} for radii larger than $60''$, respectively. The depletion radius is about $60''$. Our SO abundance is larger than the measured abundances of 4.0×10^{-10} for L1498 and 2.0×10^{-10} for L1517B, respectively. The optical depth 0.053 is taken from the RATRAN non-LTE simulation. In comparison, the constant abundance 1.0×10^{-9} extending from the core's center to its boundary was also simulated (see Fig. 4). The result revealed that the predicted intensity profile decreases radially from the center to the boundary, showing inconsistency with the observed intensity profile. In conclusion, the step function employed to describe the abundance distribution of SO in B68 demonstrates reliability, and the parameters derived through RATRAN non-LTE simulations prove to be robust.

4.3. Core-core collision scenario

From the position-velocity diagram of Fig. 5, the velocity difference between the bullet and the main body is about 0.4 km s^{-1} which is consistent with the simulated collision velocity 0.37 km s^{-1} (Burkert & Alves 2009). This provides a conclusive evidence for the bullet impacting on the main source.

In the outskirts of B68, the optical depth of SO is 0.03 estimated by RADEX under conditions of $T_K = 10$ K, $n_{\text{H}_2} = 2.0 \times 10^4 \text{ cm}^{-3}$, $N_{\text{SO}} = 1.0 \times 10^{12} \text{ cm}^{-2}$ and line width (FWHM) 0.2 km s^{-1} (van der Tak et al. 2007). Therefore, SO is optically thin and the column density is proportional to the velocity-integrated intensity. At the position of the bullet the abundance is about five times (1.0×10^{-8}) that of the abundance at the boundary. The enhanced SO towards the southeastern region (the black line in Fig. 4) is likely due to the shocks produced by core-core collision.

In addition, based on the high spatial resolution of $10''$ dust extinction data, an elongated structure has been detected towards the southeastern part of B68 (Alves et al. 2001a,b). The elongated structure is likely caused by the gravitational tidal force during the core-core collision process (Burkert & Alves 2009). As a matter of fact, SO is a good tracer to detect this kind of elongated structure caused by gravity (Lee et al. 2023). However, the elongated structure is not clearly detected by SO here probably because of the spatial resolution limitation of the data.

In summary, based on the above kinematical and chemical analyses, the SO observational results are consistent with the core-core collision scenario.

5. SUMMARY

Mapping observations of SO towards the prototypical globule B68 were conducted by the Effelsberg 100 m telescope with an angular resolution of $30''$ (0.01 pc). The results are summarized below:

(1): SO emission is detected both in the southeastern bullet and the main body of B68. The spectral line profiles are single Gaussian profiles which are quite different when being compared with the complex CS line profiles previously detected.

(2): Based on the velocity-integrated intensity map, the strongest SO emission appears at the southeastern part of B68 while the central region shows a lower surface density.

(3): Three velocity components are clearly detected based on the mapped velocity field and on the SO channel maps. The most redshifted is detected towards the southeastern bullet. Blueshifted emission is detected towards the western part, while emission at intermediate velocities is encountered towards the eastern part.

(4): The measured velocity difference between the bullet and the main core is about 0.4 km s^{-1} which is comparable with the velocity 0.37 km s^{-1} predicted by previous numerical simulations. This provides conclusive evidence for the scenario that the bullet is impacting the main core.

(5): The radial abundance profile is estimated by performing the 1D spherical non-LTE Monte-Carlo radiative transfer code RATRAN simulating the observed velocity-integrated intensity. The abundance stays constant near 2.0×10^{-9} for radii larger than $60''$. The abundance is enhanced at the interface between the bullet and the main core. This abundance enhancement is most likely caused by the shock waves produced by the core-core collision.

In conclusion, based on the kinematic and chemical analyses, the observational results suggest that the southeastern bullet is impacting on the rotating main core. This is consistent with the previously proposed core-core collision scenario in B68.

This work was funded by the National Key R&D Program of China with grant No.2023YFA1608002, by the Youth Innovation Promotion Association CAS, and by the National Natural Science foundation of

China (NSFC) under grant nos.12173075 and 12373029. It was also funded by the Chinese Academy of Sciences “Light of West China” Program under grant No. xzbzg-zdsys-202212, by the Tianshan Talent Program of Xinjiang Uygur Autonomous Region under grant No. 2022TSYCLJ00055, by the Natural Science Foundation of Xinjiang Uygur Autonomous Region under grant No. 2022D01E06, by the National Key R&D Program of China under grant No. 2022YFA1603103, by the Tianshan Talent Training Program, by the Regional Collaborative Innovation Project of Xinjiang Uyghur Autonomous Region under grant No. 2022E01050, by the Xinjiang Key Laboratory of Radio Astrophysics under grant No. 2023D04033, by the Chinese Academy of Sciences (CAS) “Light of West China” Program under grant No. 2020-XBQNXZ-017, and by the Science Committee of the Ministry of Science and Higher Education of the Republic of Kazakhstan with grant No. AP13067768. K.W. and T.L. are supported by the Tianchi Talent Program of Xinjiang Uygur autonomous region. C.H. and A. S. have been funded by Chinese Academy of Sciences President’s International Fellowship Initiative grants nos.2025PVA0048 and 2024VMA0002, respectively.

REFERENCES

- Alves, F. O., & Franco, G. A. P. 2007, *A&A*, 470, 597
- Alves, J., Lada, C., & Lada, E. 2001a, *The Messenger*, 103, 1
- Alves, J. F., Lada, C. J., & Lada, E. A. 2001b, *Nature*, 409, 159
- Barnard, E. E. 1919, *ApJ*, 49, 1
- Bergin, E. A., Alves, J., Huard, T., & Lada, C. J. 2002, *ApJL*, 570, L101
- Bergin, E. A., & Tafalla, M. 2007, *ARA&A*, 45, 339
- Blake, G. A., Sutton, E. C., Masson, C. R., & Phillips, T. G. 1987, *ApJ*, 315, 621
- Bok, B. J., & Reilly, E. F. 1947, *ApJ*, 105, 255
- Bonnor, W. B. 1956, *MNRAS*, 116, 351
- Burkert, A., & Alves, J. 2009, *ApJ*, 695, 1308
- Chandrasekhar, S. 1967, *An introduction to the study of stellar structure*
- Chuang, C.-Y., Aso, Y., Hirano, N., Hirano, S., & Machida, M. N. 2021, *ApJ*, 916, 82
- Codella, C., & Muders, D. 1997, *MNRAS*, 291, 337
- Comito, C., Schilke, P., Phillips, T. G., et al. 2005, *ApJS*, 156, 127
- de Geus, E. J., de Zeeuw, P. T., & Lub, J. 1989, *A&A*, 216, 44
- Ebert, R. 1955, *ZA*, 37, 217
- Friberg, P. 1984, *A&A*, 132, 265
- Goodman, A. A., Benson, P. J., Fuller, G. A., & Myers, P. C. 1993, *ApJ*, 406, 528
- Goodman, J., & Weare, J. 2010, *Communications in Applied Mathematics and Computational Science*, 5, 65
- Heithausen, A., Corneliussen, U., & Grossmann, V. 1995, *A&A*, 301, 941
- Hogerheijde, M. R., & van der Tak, F. F. S. 2000, *A&A*, 362, 697
- Hotzel, S., Harju, J., & Juvela, M. 2002, *A&A*, 395, L5
- Keto, E., Broderick, A. E., Lada, C. J., & Narayan, R. 2006, *ApJ*, 652, 1366
- Lada, C. J., Bergin, E. A., Alves, J. F., & Huard, T. L. 2003, *ApJ*, 586, 286
- Lada, C. J., Lada, E. A., Clemens, D. P., & Bally, J. 1994, *ApJ*, 429, 694
- Lai, S.-P., Velusamy, T., Langer, W. D., & Kuiper, T. B. H. 2003, *AJ*, 126, 311
- Lee, J.-E., Matsumoto, T., Kim, H.-J., et al. 2023, *ApJ*, 953, 82
- Li, D., Lou, Y.-Q., & Esimbek, J. 2018, *MNRAS*, 473, 2441

- Lique, F., Dubernet, M. L., Spielfiedel, A., & Feautrier, N. 2006, *A&A*, 450, 399
- Lombardi, M., Alves, J., & Lada, C. J. 2006, *A&A*, 454, 781
- Maret, S., Bergin, E. A., & Lada, C. J. 2007, *ApJL*, 670, L25
- Martin-Pintado, J., Bachiller, R., & Fuente, A. 1992, *A&A*, 254, 315
- McKee, C. F., & Ostriker, E. C. 2007, *ARA&A*, 45, 565
- Redman, M. P., Keto, E., & Rawlings, J. M. C. 2006, *MNRAS*, 370, L1
- Rydbeck, O. E. H., Hjalmarson, A., Rydbeck, G., et al. 1980, *ApJL*, 235, L171
- Schilke, P., Groesbeck, T. D., Blake, G. A., Phillips, & T. G. 1997, *ApJS*, 108, 301
- Schmid-Burgk, J., Henkel, C., Hüttenmeister, S., et al. 1992, in *Astronomische Gesellschaft Abstract Series*, Vol. 7, 46–46
- Schmid-Burgk, J., & Muders, D. 1994, in *Astronomical Society of the Pacific Conference Series*, Vol. 57, *Stellar and Circumstellar Astrophysics, a 70th birthday celebration for K. H. Bohm and E. Bohm-Vitense*, ed. G. Wallerstein & A. Noriega-Crespo, 74
- Tafalla, M., Santiago-García, J., Myers, P. C., et al. 2006, *A&A*, 455, 577
- van der Tak, F. F. S., Black, J. H., Schöier, F. L., Jansen, D. J., & van Dishoeck, E. F. 2007, *A&A*, 468, 627
- Winkel, B., Kraus, A., & Bach, U. 2012, *A&A*, 540, A140

APPENDIX

A. BONNER-EBERT SPHERE

For a spherical ideal gas system with gravity and thermal pressure, the system under balance can be described by the Lane-Emden equation. For the isothermal Lane-Emden equation (Chandrasekhar 1967),

$$\frac{1}{\xi^2} \frac{d}{d\xi} \left(\xi^2 \frac{d\psi}{d\xi} \right) = \exp(-\psi), \quad (\text{A1})$$

where $\xi = (r/C_s)\sqrt{4\pi G\rho_c}$ is the non-dimensional radius, r is the dimensional radius, G is the gravitational constant, ρ_c is the mass density at the origin, $C_s = \sqrt{k_B T/(\mu m_H)}$ is the sound speed, k_B is the Boltzmann constant, T is the kinetic gas temperature, μ is the mean molecular weight of the gas and m_H is the hydrogen mass, and $\psi(\xi) = -\ln(\rho/\rho_c)$, ρ is the mass density. The boundary conditions of equation (A1) are $\psi(0) = 0$ and $d\psi(0)/d\xi = 0$. Then, the equation (A1) can be numerically solved. For a finite radius hydrostatic system, the system can be described by a truncated Lane-Emden equation also called Bonnor-Ebert Sphere (Bonnor 1956; Ebert 1955). The maximum non-dimensional radius $\xi_{\max} = (R/C_s)\sqrt{4\pi G\rho_c}$, where R is the radius of the system. Bonnor (1956) and Ebert (1955) studied the stability of the truncated Lane-Emden equation. They found the system is expected to be gravitational unstable when $\xi_{\max} > 6.5$. For B68, the density structure can be well fitted by the Lane-Emden equation with the $\xi_{\max} = 6.9$ indicating that B68 is unstable (Alves et al. 2001b).

B. PROCEDURE FOR SOLID-BODY ROTATION FITTING

The emcee code is run by sampling the posterior probability function to conduct the MCMC procedure. The posterior probability function consists of two components: a likelihood function and a prior function. A Gaussian function is adopted as the likelihood function. Therefore, the log likelihood function is defined as $-0.5 \times (v_{\text{obs}} - v_{\text{model}})^2 / v_{\text{error}}^2$, where v_{obs} represents the observed velocity field (i.e., moment-1), v_{model} is the theoretical velocity field calculated from eq.(1), and v_{error} denotes the uncertainty of the observed field v_{obs} . The typical velocity uncertainty v_{error} was calculated as 0.011 km s^{-1} through error propagation analysis based on the spectra baseline noise level. The prior function is assumed to follow a constant probability distribution. The parameter ranges are set as follows: v_{sys} from 3 to 4 km s^{-1} , dv/ds from 1 to $4 \text{ m s}^{-1} \text{ arcsec}^{-1}$ and θ from -1 to 6° . To run the emcee, the parameters nwalkers and steps are set to 32 and 5000, respectively. The calculated autocorrelation time is [37, 35, 38]. The posterior distributions of the three fitted parameters are presented in Fig. 6.

To evaluate whether the solid-body rotation model is appropriate, Fig. 7 displays the observed velocity field, the modeled velocity field derived from the best-fit parameters, and the residual distribution generated by subtracting the model from the observed velocity field. The residual distribution exhibits remarkable smoothness, with residual values confined to a narrow range of -0.08 to 0.08 km s^{-1} . These results demonstrate that the solid-body rotation model is appropriate to describe the velocity field in the main body of B68.

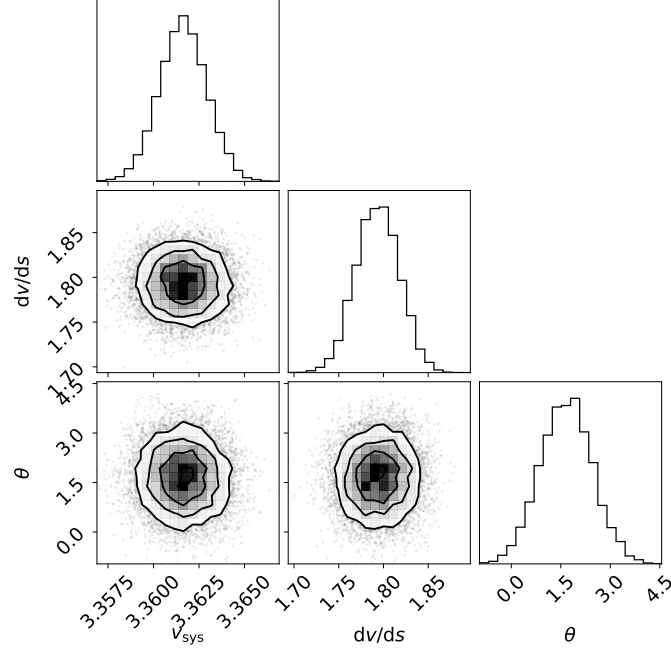


Figure 6. The best-fitting results. The posterior distributions of the three fitted parameters v_{sys} , dv/ds in $\text{ms}^{-1} \text{arcsec}^{-1}$, i.e. the systemic velocity, the velocity gradient, and the direction of the gradient (see eq.(1)).

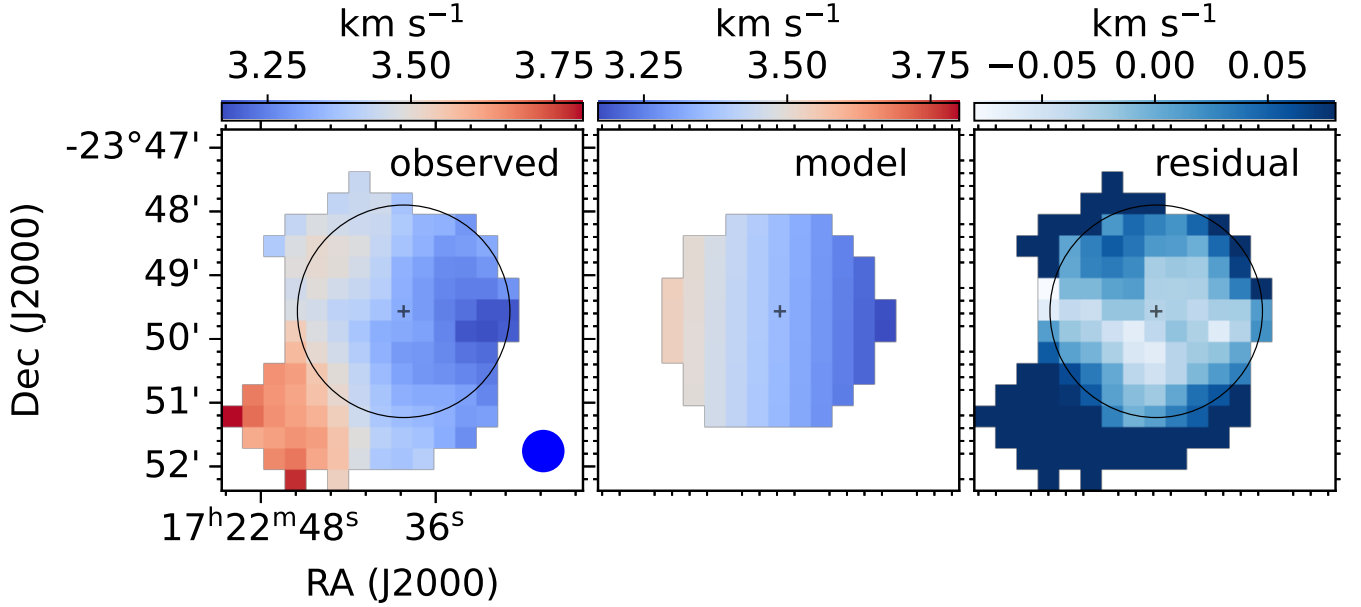


Figure 7. Solid-body rotation model assessment. The left panel shows the observed velocity field. The middle panel displays the modeled velocity field derived from the best-fitting parameters. The right panel presents the residual produced by subtracting the model from the observed velocity field.